THAPATHALI CAMPUS
Institute of Engineering
Tribhuvan University

Development and application of a high-speed reacting flow solver in OpenFOAM

Sanjeev Adhikari[a], Hao Tang[a,*] and Sudip Bhattrai[b]

[a]College of Energy and Power Engineering, Nanjing University of Aeronautics and Astronautics, Nanjing 210016, PR China

[b]Department of Mechanical and Aerospace Engineering, Institute of Engineering Pulchowk, Tribhuvan University, Chakupat, Pulchowk, Lalitpur-44700, Nepal

ARTICLE INFO

Abstract

A numerical study was conducted to verify and validate a new solver, named *hyperReactingSodFoam*, based on the OpenFOAM toolbox. This study mainly focuses on verifying the solver's computational capability to compute hypersonic flows involving shock-induced combustion, and its applications. This investigation is limited to inviscid flow and incorporates Minmod limiter to achieve total variation diminishing property. Analysis of a practical case was conducted by simulating and validating hypersonic blunt body projectile experiments at Mach 6.46 and 4.18. Likewise, to demonstrate the wider applicability of solver, a standing detonation in an oblique detonation wave engine; combustor with a sharp as well as a blunted wedge geometry was studied. It was observed that, for a given flow condition and combustor geometry, a sharp wedge has a better mass-weighted average pressure recovery comparative to the blunted wedge. However, blunted wedge geometry provides a better picture of the detonation phenomenon as a practical wedge will have finite bluntness. In addition, the concept of the detonation induction length becomes less relevant for a blunted wedge.

1. Introduction

The OpenFOAM open-source toolbox serves as a unique computational fluid dynamics (CFD) platform to develop solvers with its programming tools based on C++. It contains a wide range of modules assembled to solve numerical problems expressed by ordinary differential equations or partial differential equations. The toolbox has in-built physical modules describing flows that are incompressible, compressible, reacting, radiative, etc., and provides an easy and efficient implementation system to build a new solver. In addition, its availability to parallelization provides enormous benefits in making computation more robust.

This study utilizes verified utilities within OpenFOAM and carries on from other validated solvers developed in the OpenFOAM toolbox to create a new solver that can reliably compute high-speed reacting flows. There are currently a limited number of density-based solvers implemented in OpenFOAM that are freely accessible for performing robust solutions of supersonic/hypersonic reacting flows. The current version of the previous in-house solver *hyperReactingFoam* [1], [2] is based on *rhoCentralFoam* [3], *ddtfoam* [4], and *densityBasedTurbo* [5] solvers, which used Riemann type schemes to compute fluxes at the cell center. The previous version of this solver has successfully evaluated Oblique Detonation Waves (ODWs) characteristics in a ramp geometry [1], [2]. However, its failure to calculate ODWs in blunt geometry drives the improvement of the existing numerical computation techniques in the solver. Therefore, this paper provides details on implementing significant changes in the interpolation of cell center primitive variables, such as p, ρU, ρE, etc., into face flux. In addition, it also adopts computation of convective fluxes for species using the generic Riemann Scheme instead of evaluating using the OpenFOAM module. Thus, this upgrade increases the spatial accuracy of the solver to second order. We anticipated that the new solver would efficiently compute the detonation phenomenon in any complex geometry by successfully implementing the

*Corresponding author:
✉ hao.tang@nuaa.edu.cn (H. Tang)

techniques mentioned above in the new solver. It would eventually increase the research regarding detonation at high speeds without being limited to complex geometry, which would ultimately play a crucial role in developing a practical Oblique Detonation Wave Engine.

Recent developments in experimental facilities that can produce standing ODWs Rosato et al. [6] have opened a new window for hypersonic propulsion systems development. In the past three decades, different experimental [7], [8] and numerical studies [9], [10] carried out in ODWs mainly focus on the simple infinite wedge geometry. Whereas some studies [2], [11], [12], [13] have focused on the complex geometry, which explores an expansion corner connecting to the nozzle. Previously, [14], [15], [16] studied ODWs computationally in a ramjet where initiation of detonation waves was primarily due to reflected Oblique Shock Wave from the wall, where induction region originates due to an increase in the temperature and pressure after each reflection shock wave. They also confirm that the combustion chamber thermally chokes for a certain inlet Mach number. In this case, the expansion wave interacts with reflected shock waves, weakening shock strength. However, such a phenomenon requires further computational studies, looking at the effect of ODWs reflections and interactions with expansion waves. Similarly, Sislian et al. [17] carried out a numerical analysis on the performance of a ramjet engine with a relatively complex geometry, which incorporated lower and upper expansion corners connecting to the nozzle. The results showed a novel phenomenon leading to distortions of the ODW near the reflection wall. However, the research did not address the detailed physics of such a phenomenon.

Most of the recent studies [10], [18], [19] performed with an infinite-length wedge demonstrates ODW formation, structure, and stability conditions successfully. Previously, mainly two distinct wave structures, i.e., smooth and abrupt, have been observed. At low inflow Mach numbers, Teng et al. [18] observed a complex wave structure composed of Mach stem attached with λ shock below the inflexion. Similarly, Teng et al. [20] observed Y and X-shaped structures of the ODW induction region, where the X-shaped structure transformed into a Y-shaped structure. In this region, the inflow Mach number was a specific parameter that determined the dominance of OSW or ODW in the induction region. Papalexandris et al. [11] investigated finite-length wedges, including expansion corners, and concluded that the expansion wave does not affect the ODW that formed upstream simply a characteristic of supersonic flows. However, for ODWs that formed downstream of the expansion corner, effects on the inflexion of ODW were observed. Similarly, they showed that the expansion wave

might also weaken the ODW up to a Chapman-Jouguet wave for some specific geometrical or flow conditions. Bomjan et al. [2] also studied finite-length wedges with small expansion steps to show that the interaction of expansion waves and ODWs results in the decoupling between the OSW and the reaction front. Verrault et al. [21] experiment depicts five different combustion regimes: spontaneous ODW, delayed ODW, combustion instabilities, decoupled shock and reaction front, and inert shock wave. This study found that the total energy and rate at which energy is released are critical parameters for the initiation of detonation from a conical projectile. Thus, in case of initiation of prompt detonation from the blunt cone for a decreasing cone angle, transient regime: prompt ODW, delayed ODW, and non-reacting shock is more vivid, whereas for decreasing mixture pressure transient regime as prompt ODW, combustion instabilities, and non-reacting shock are seen. Moreover, the decoupled regime was observed as bow shock was not sufficiently strong enough to sustain a spontaneous ODW (originated at cone tip) in the farfield. These studies cover the current understanding of the ODW formation and decoupling phenomena and form the bulk of the contemporary ODW literature.

A concerted investigation by Fujiwara et al. [22] on blunt bodies showed that at high Mach numbers, the bow-shock wave over the blunt leading-edge is closely coupled with the reaction front, while a converse phenomenon occurs at low Mach numbers, except in the stagnation region where we observed a normal detonation. In this, case parameters like the radius of bluntness, wedge angle, Mach number, exothermicity, and rate of chemical reaction, defined the stability of the standing detonation waves. Recently, Fang et al. [23] illustrated two different kinds of initiation in a blunt wedge geometry. The first of these initiation methods occur at the stagnation region due to blunt geometry, while the second initiates downstream due to the OSW compression over the flat wedge surface.

In an early experimental investigation of blunt body projectiles, Lehr et al. [24] stated that bow shock formed in front of the blunt-body induces the detonation wave. They showed that the induction length depends on the strength of the bow shock. The induction length gradually increases at low Mach numbers, eventually resulting in shock-induced combustion. The authors also inferred that underdriven detonations are unstable and periodic. McVey and Toong et al. [25] investigated regular, periodic instabilities in the exothermic hypersonic blunt body reacting flows. Their one-dimensional wave model demonstrated that the induction region is the origin of the instability caused by the induction time of entropy

waves. The study explained that the generation of entropy waves occurs when compression waves interact with the bow shock. However, Matsuo et al. [26], in a detailed numerical analysis, concluded that compression wave reflected on the stagnation point of the blunt-body is also the reason for instabilities, and not only the wave interaction between the compression waves and the bow shock. Their experiments also showed that the expansion wave quenches the detonation waves, resulting in a decoupled bow shock and reaction front. Moreover, other numerical studies [26], [27], [28], [29], [30] based on the experimental cases by Lehr et al. [24] validate the computational method and chemical kinetics model [31] to capture the detonation waves with high accuracy. These studies also investigated the transient nature of underdriven detonation waves. Even though previous studies [24], [25], [26], [27], [28], [29], [30] have investigated initiation of detonation waves due to blunted projectiles, comparatively less research has been conducted on blunted wedge geometries. This is despite the fact a practical vehicle geometry has unavoidable bluntness and rounded corners arising from manufacturing accuracy and tolerances, as well as material limitations that hinder machining of sharp edges.

Relying on the previous numerical studies and the experiments by Lehr et al. [24], this paper describes modifications in numerical computation techniques, i.e., reconstruction method and connective fluxes evaluation for each species using the Riemann scheme implemented in the current solver. It also provides validation and verification results obtained with experimental and numerical results. Therefore, the comparison of the current solver is not limited to the previously obtained numerical results. To validate the solver utility, we considerate the experimental cases of Lehr et al. [24]. The current study also successfully demonstrates the applicability of the present solver to compute the ODWs over both a sharp wedge, and blunt-wedge geometries.

2. Numerical Methods

In the solver, a set of two-dimensional Euler equations for an unsteady compressible reactive flow is solved using the second-order spatially accurate new solver hyperReactingSodFoam (hRSF). The conservation form of the governing equation are formulated as follows:

$$\frac{\partial \rho}{\partial t} + \nabla \left(\vec{\phi} \right) = \quad 0 \tag{1}$$

$$\frac{\partial \left(\rho \vec{U} \right)}{\partial t} + \nabla \left(\vec{\phi} \vec{U} \right) = \quad -\nabla p \tag{2}$$

$$\frac{\partial \left(\rho E \right)}{\partial t} + \nabla \left(\vec{\phi} H \right) = \quad 0 \tag{3}$$

$$\frac{\partial \left(\rho Y_i \right)}{\partial t} + \nabla \left(\vec{\phi} Y_i \right) = \quad \dot{x}_i W_i \tag{4}$$

Here, $E = e + \frac{1}{2} U^2 + \frac{p}{\rho}$ is total energy, $H = E + \frac{p}{\rho}$ is the total enthalpy. $AUSM+up$ scheme [32] was implemented to compute the numerical fluxes such as convective face flux $\vec{\phi} = \rho \vec{U}$, energy density flux $\vec{\phi} H$, and species density flux $\vec{\phi} Y_i$ for each species. Equation of state for the perfect gas mixture Equation 5 encloses the above numerically stiff set of Equations 1, 2, 3, and 4, which makes it possible to fully solve the inviscid reactive flow field numerically.

$$p = \quad \rho R T \sum_i \frac{Y_i}{W_i} \tag{5}$$

Correspondingly, Y_i is the mass fraction of the chemical species i, and $\dot{x}_i W_i$ is the reaction source term, where W_i and $\dot{x}_i$ represent the molecular weight of the species and specie molar production rate, respectively. For each elementary reaction, reaction rate constants k is computed through Arrhenius law,

$$k = \quad A T^\beta exp^{(-E/RT)} \tag{6}$$

Here, the widely used *H2-air* chemical reaction mechanism [31] for numerical computation of blunt body projectiles in a detonable gas mixture is selected. The reduced reaction mechanism consisting of N_2 as inert species from Jachimowski's 33 step-model considers a 9 species [$O_2, H, OH, O, H_2, H_2O, N_2, HO_2, H_2O_2$] with 19 reversible elementary reactions as taken for the study of detonation in blunt projectile by Wilson et al. [28]. The reaction rate k and $\dot{x}_i$ molar production rate is computed utilizing the CHEMKIN package. Thermodynamic properties of chemical species are obtained from the 7-coefficient NASA polynomial representation [33].

2.1. Reconstruction at interference

Convective fluxes at the face interface are calculated with first-order spatial accuracy using a Riemann type scheme, i.e., $AUSM+Up$. Reconstruction of the primitive variables at the cell center to face interface improves the spatial order of accuracy of the fluxes. Taylor series expansion was adopted in the previous version of the current solver, like the *ddtFoam* [4] and *densityBasedTurbo* [5] solvers, to extrapolate the primitive variables at the face interface. Mathematically second-order Taylor series is expressed as:

$$\Psi_f = \Psi + (\Delta \vec{r} \, \nabla \Psi)_n \tag{7}$$

where, Ψ represents the primitive variables flux density, subscript f represents interface face (Left/Right), $\Delta \vec{r}$ is the distance between the interface and cell center, $\nabla \Psi$ is the gradient of the primitive variables, and $n = 2$ for second-order extrapolation. Though the Taylor series is spatially second-order accurate, it cannot resolve the spurious oscillations and excessive diffusion resulting in a non-physical solution. A new formulation technique presented in *rhoCentralFoam* [3] is adopted to resolve this issue, which conserves the Total Variation Diminishing (TVD) property. This reconstruction technique is more generalized as we can use it for unstructured and nom-orthogonal structured meshes. So, it is more advantageous to compute unstable detonation cases with complex geometry.
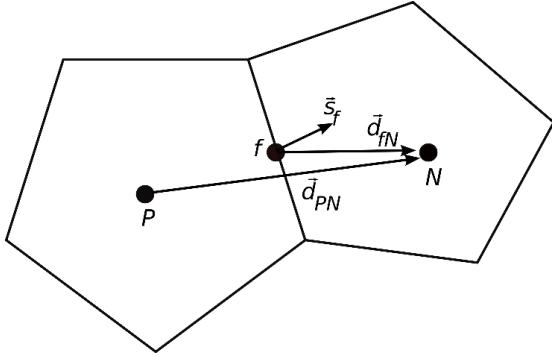
Figure 1: Polyhedral domain discretization

The schematic diagram in Figure 1 shows an unstructured grid P and N represents the cell center, f is the interface face, and $\vec{S}_f$ is a vector normal to the interface f directed out of point P. Similarly, $\vec{d}_{PN}$ connects the cell centers of two grid cells while $\vec{d}_{fN}$ connects the face center to the grid cell center N on the right. In this technique, interface fluxes directed from cell center P to cell center N are positive and vice-versa. So, the interpolation function Ψ for a primitive variable is obtained as

$$\Psi_{f_\pm} = (1 - \alpha_{f_\pm})\Psi_P + \alpha_{f_\pm}\Psi_N \tag{8}$$

Where, $\alpha_{f_+} = \beta(1 - w_f)$, $\alpha_{f_-} = \beta w_f$ and limiter function $\beta(r)$ differentiate the selection of TVD and symmetric properties. w_f represents the weighting coefficient, i.e., $w_f = \vec{d}_{fN}/\vec{d}_{PN}$. We utilize Minmod limiter [34] for this study and is computed as $\beta(r) = max\,[0,\,min(1,r)]$. The flux limiter function $\beta(r)$ acts as the bridge that enables a switch between low- and high-order schemes, where the ratio of consecutive gradients of interpolated variable (r) is limited,

i.e., $r \geq 0$. Mathematically, the computation of (r) for scalar and vector primitive variables is carried out with Equation 9 and 10, respectively.

$$r = 2\frac{\vec{d}_{PN}(\nabla\Psi)_P}{(\nabla_{PN}\Psi)_f} - 1 \tag{9}$$

$$r = 2\frac{(\nabla\Psi)_f \, \vec{d}_{PN}(\nabla\Psi)_P}{(\nabla_{PN}\Psi)_f \, (\nabla_{PN}\Psi)_f} - 1 \tag{10}$$

Here, $(\nabla\Psi)_P$ is the full-gradient calculated at the cell P as shown in Figure 1 and $(\nabla_{PN}\Psi)_f = \Psi_N - \Psi_P$ is the scaled (by $\vec{d}_{PN}$) gradient component normal to the face.

2.2. Species flux
In the previous version of the current solver, species transport Equation 4 was computed using the Open-FOAM module, whereas other convective fluxes were calculated using the Riemann scheme. Therefore, to improve the spatial order of accuracy of the species flux density, mathematically, it is computed using the Riemann scheme, i.e., *AUSM+up* as,

$$\phi Y_i = \left(\frac{1}{2}(U(\rho Y_{Li} + \rho Y_{Ri})) - |U|(\rho Y_{Ri} - \rho Y_{Li})\right)|\vec{S}_f| \tag{11}$$

Where subscripts Li/Ri represents the Left/Right values of the reconstructed field for each species. Thus, computed fluxes are spatially second-order accurate.

2.2.1. Implementation
The above mathematical formulation is implemented in the generic Riemann flux class in OpenFOAM, creating two objects, pos and neg, representing flux from P to N and vice versa, as shown in Figure 1. These two objects are assigned with positive and negative scalar units, as implemented in the solver *rhoCentralFoam* [3]. As mentioned earlier, the interpolation function defined in Equation 8 is implemented in the generic Riemann flux class for each primitive variable explicitly where pos or neg determines the flux direction.

As mentioned in section 2.2 to implement the mathematical form of species density fluxes Equation 11, all the species are first initialized in the *RiemannFlux* class. Similarly, *rhoScalarFlux*, *gradrhoScalar*, and *rhoYLimiter*, corresponding to the classes, *surfaceScalarField*, *volVelctorField*, and *volScalarField*, respectively, are added into the constructor function class and is initialized before they are called in the member function. Thus, initialized first order spatially accurate species density

at the cell center using the generic Riemann class is interpolated to the face interface preserving a TVD property which eventually increases spatial accuracy to second order. The explicitly computed scalar flux density is accessed while solving the species transport equation.

Similarly, for parallelization of the above implementations, adopted in the generic class code after was conducted out after confirming the *boundaryField* is a coupled face. Otherwise, a non-coupled face function was used for all primitive variables. Parallelization is implemented for all primitive variables and acoustic speed in the generic Riemann flux Class. Thus, the new version of the solver is referred to as *hyperReactingSodFoam* (hRSF).

3. Results and Discussion

The main objective of the changes implemented in the current solver was to resolve supersonic/hypersonic reacting flows with greater precision and robustness. We selected a detonation case initiated by a blunt body projectile to demonstrate its capability further. We consider the experimental cases from Lehr et al. [24] performed at two different Mach numbers: Mach 6.46 and Mach 4.18, at T = 292 K and p = 42.6 kPa. These two Mach numbers were considered such that they capture the solver's capabilities to compute two different natures of the detonation phenomena induced by a blunt body, namely:

(1) Stable and overdriven detonation waves.

(2) Unstable and underdriven detonation waves.

An axisymmetric computational domain with a blunt body diameter of 15 mm was considered, replicating the experimental case. Geometry was revolved at a half-cone of 2.5° on both sides from the centerline to create the axisymmetric domain in OpenFOAM, which is a standard angle for wedge boundary conditions imposed on the right and left sides. The domain inlet was set as a fixed-velocity inlet with the inflow stoichiometric premixed H2-air mixture at a ratio of $H_2 : O_2 : N_2 = 2 : 1 : 3.76$. *Zero-gradient* boundary conditions were imposed at the outlet for scalar variables, while the extrapolated *inletOutlet* boundary conditions were applied for the velocity field. Wall of the domain was set to *slip* boundary condition for vector field while *zero-gradient* condition was used for scalar fields. It should be noted that throughout this research viscous nature of the flow is neglected, considering that the effect of a boundary layer is negligible.

3.1. Overdriven detonation wave
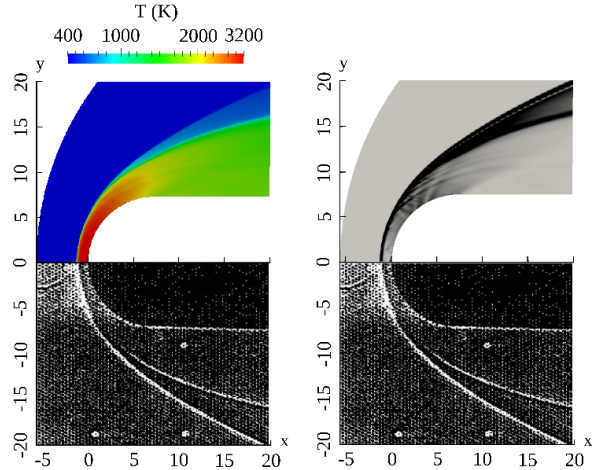
Figure 2: Experimental schlieren [24] and numerically obtained temperature contour and density gradient at Mach 6.46.

As explained earlier, Lehr et al. [24] experimental case at Mach 6.46 was considered to accurately demonstrate the solver's capability to capture bow shock and the reaction front. The numerical results obtained show that that solver accurately computes the bow shock wave and reaction front, as shown in Figure 2. The above figure illustrates that the bow shock stand-off distance matches the experimental results. It was found that simulation was stable, and no spurious oscillations were initiated from the stagnation line. To further demonstrate the computational capability of the developed solver, we carried out a comparative study with other previous numerical validation analyses of detonation induced by a blunt body projectile.

For this investigation, pressure, temperature, and density fields along the computational domain's stagnation line were analyzed after the solutions were fully developed and stable detonations were formed. The results obtained were plotted alongside the results from Yungster & Bruckner et al. [29] at Mach 6.46 flow condition, as shown in Figure 3. These plots show that hRSF computes the shock stand-off distance with a significantly greater spatial resolution. The authors also mentioned the issue with a thick and diffused bow shock in Yungster & Bruckner et al. [29] while comparing their numerical results with Lehr's experimental results. Similarly, the plots in Figure 3 (b) and (c) also illustrate that the flow parameters at the stagnation point are comparatively higher for hRSF solution. Due to the differences in flux computation schemes, hRSF uses the pressure flux correction method. Further investigation showed that the above results are independent of the numerical grids. Grid Convergence Index (GCI) and order of convergence p' were analyzed to verify the numerical

accuracy of the simulations.
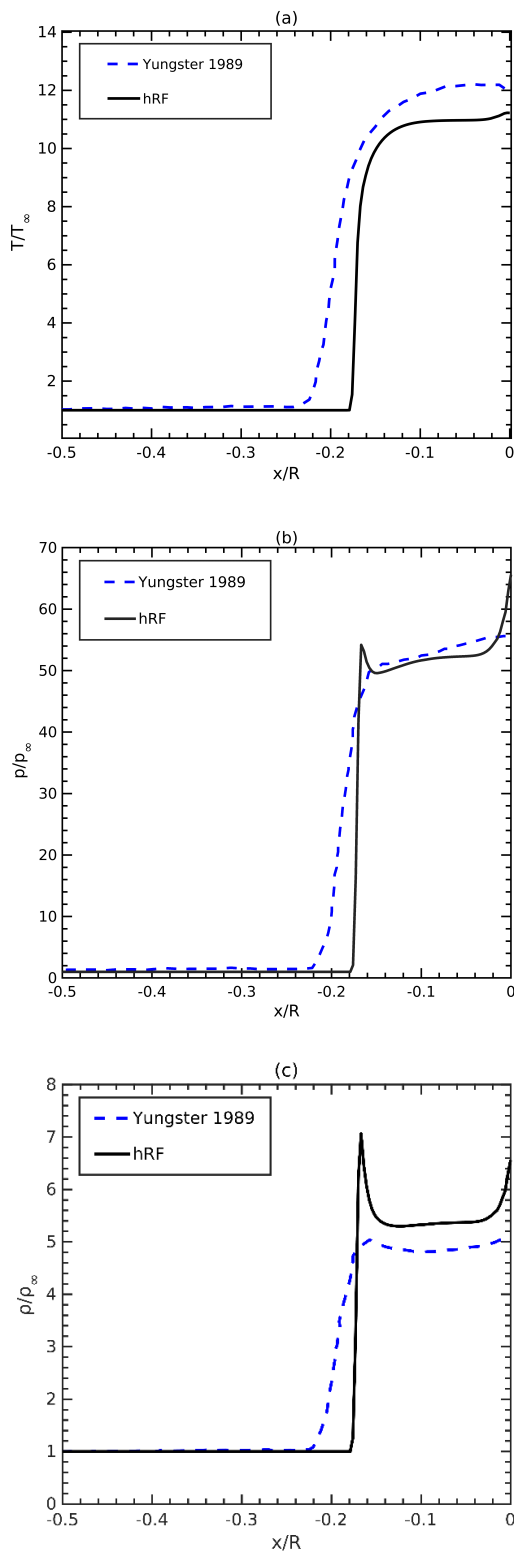
Figure 3: Experimental Comparative plot between two results obtained computationally (a) temperature ratio (b) pressure ratio (c) density ratio.
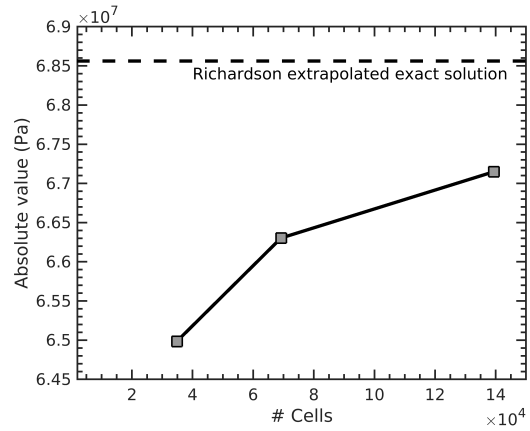
Figure 4: Grid convergence study along with Richardson extrapolated exact solution.

For GCI investigation, the total pressure at the outlet was extracted, with an increasing trend of total pressure with the increase in the number of cells as shown in Figure 4. From this plot, we can infer that for infinite number of cells, value of total pressure asymptotes with an exact solution represented by Richardson's extrapolation. The computed value of p' was 1.34. The grid adopted for the current simulations was the finest mesh size from the analysis, shown on the far right-hand side of Figure 4.

3.2. Underdriven detonation wave
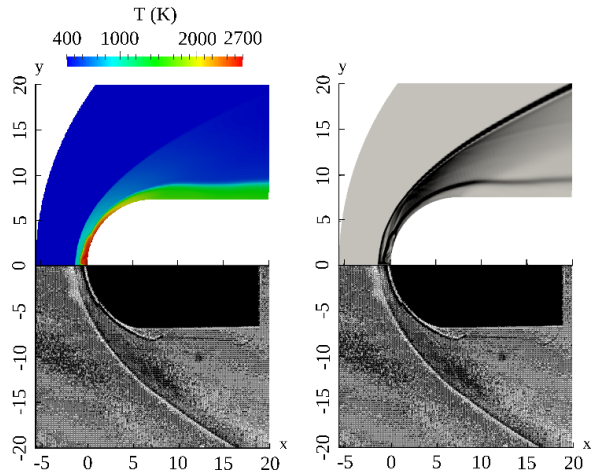
Figure 5: Experimental schlieren [24] and numerically obtained temperature contour and density gradient at Mach 4.18.

To further demonstrate the usability of the current solver, the unstable and underdriven detonation case from Lehr et al. [24], at Mach 4.18 condition, was simulated as shown in Figure 5. The experimental result and the simulation contour resemble closely. We observed that

the low Mach number induction length is larger than the Mach 6.46 case analyzed in the previous section. There is a close coupling between the bow shock and the reaction front at the higher Mach number, unlike for Mach 4.18. This case is highly unstable, and we also observed that a high-temperature zone representing the combustion region along the wall of the domain occurs at a specific frequency. We inspected the small kink formation near the stagnation line in Figure 5, and we observed that this occurred as the solver is first-order accurate in time. This leaves a necessity to improve the solver further. We assume upgrading first-order time integration to Runge-Kutta third-order will phase out such small kink formations at the stagnation region.

4. Solver Application: ODWE Combustor

An ideal application of the solver is the simulation of an oblique detonation wave engine (ODWE) combustor channel. Such a channel may be formed of a ramp inclined against the incoming premixed fuel-air mixture flow at an angle above the Chapman-Jouguet turning angle. The combustor geometry forms a standing ODW, where the detonative combustion leads to instantaneous heat release. This results in a high combustion efficiency and a significantly short combustor length. This section intends to provide an example for the current solver, which will form a broader study in the future utilizing the solver. The example is related to an ODW induced by a blunt wedge, and it gives a preliminary concept of how the current solver can be utilized to investigate practical ODWE combustors.

A persevering question in the ODWE research is with regards to the geometry of the combustor that can deliver the best combustion and aerothermodynamic performance at the lowest possible length required for complete combustion and heat release. Therefore, a broader question the current research intends to tackle is the effect of various geometrical parameters on the combustor performance. In this study, a combustor geometry with a centerline wedge was selected to form a practical test case for an ODWE. The combustor with height of 100 mm and the wedge half angle of 21° was selected based on Rankine-Hugoniot analysis and exploratory simulations. The wedge was simulated as having an infinite inclined surface length to analyze purely the leading-edge bluntness effects. The stoichiometric H2-Air mixture's inflow Mach number is 6.0, with static temperature and pressure of 650 (K) and 42.6 (kPa).

The result for a combustor with an infinitely sharp wedge, using the current solver, is shown in Figure 6. The figure shows pressure and temperature contours

from the simulation, along the general dimensions of the domain. The results show the induction method of an ODW over a flat wedge. The induction process involves a gradual increase in pressure aft of the oblique shock wave, followed by a sudden jump of the flow properties once the ODW emanates from a triple-point structure.

An important aerothermodynamic performance parameter for the combustor is the total pressure recovery that is the outlet-to-inlet ratio of the total pressures. The inflow total pressure of the combustor is 77.1 MPa, with a uniform flow at the inlet, while the mass-flow-averaged total pressure at the outlet of the combustor with a sharp wedge in Figure 6 is 15.6 MPa. This gives the total pressure recovery of the combustor of 0.202. On the other hand, the mass-weighted-average compression ratio across the ODW for this combustor is 11.34, with peak compressed, burnt gas temperature of around 3000 K. The total pressure recovery of an ODWE combustor is lower than for diffusive or shock-induced combustion modes in a scramjet, which is a major impediment for its application at lower hypersonic Mach numbers.

On top of this, any practical wedge has a finite leading-edge bluntness due to manufacturing reasons. In addition, it is desirable to have a finite leading-edge bluntness to maintain the integrity of the wedge at thermal and pressure loadings. Therefore, the blunt wedge case studied here explores the deviation of the ODW properties from that of a sharp wedge. We take a blunt wedge of a 3 mm radius bluntness for this study, keeping the rest of the computational height and length the same as the sharp-wedge domain. The bluntness radius was selected based on the theoretical analysis of critical radius as proposed by Fang et al. [23], which concluded that for the initiation of prompt detonation at the leading-edge, the radius of bluntness must be greater than the critical radius.

Moreover, the radius of bluntness for the particular case presented in this study was maintained larger enough so that detonation initiated at the leading-edge is sufficiently strong enough to sustain downstream. Otherwise, for a smaller but larger than the critical radius, we can observe decoupling of reaction front and shock as previously depicted by studies [21] and [23] for blunt cone and blunt wedge. Similarly, as concluded by Fang et al. [23], for such cases, type II initiation, i.e., initiation of ODW over a wedge aft downstream of decoupling region, can be seen.

The blunt wedge induces an instantaneous detonation forming at the blunted leading-edge, owing to a strong normal shock. Such a case is shown in Figure 7, with a combustor of the same dimensions as the sharp wedge.
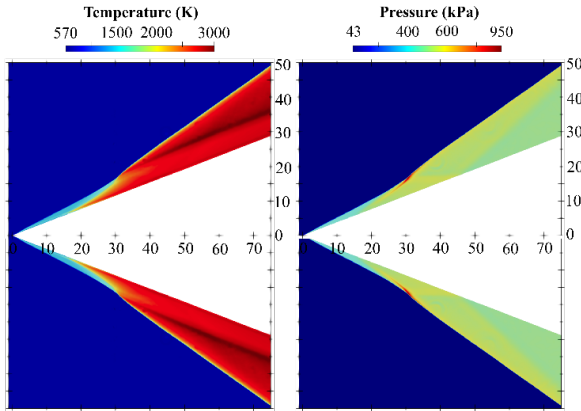
Figure 6: ODWE combustor with a sharp wedge.

Figure 7: ODWE combustor with a blunted wedge.

(The inlet shape was selected based on simulation efficiency and has no effect on the simulation results.) As mentioned earlier, we can notice that detonation initiated at the leading-edge sustains downstream; thus, we can observe a standing oblique detonation wave for this case. Moreover, detonation wave angle is greater than detonation over a sharp-wedge; therefore, for the same confined combustor dimension, we can notice the higher-pressure region at the upper and lower wall boundary due to the impingement of detonation wave. To avoid such a phenomenon, we can either raise the height of the domain or add a nozzle geometry as represented in a previous study [17]. However, this research focuses on the comparative difference in pressure recovery in a blunt and sharp wedge confined domain of the same size and distinguishes the initiation nature of detonation. Even though the flow field of combustor chamber connected with the nozzle is not primarily focused in this study, the current solver can simulate such a region efficiently.

The mass-weighted- average total pressure recovery of the combustor is 0.126, which is significantly lower than the sharp-wedge case. This indicates the significant deviation of the combustor performance resulting from a practical bluntness of the wedge. Of course, the required bluntness may be smaller, which can be more conservative of the combustor performance. The mass-weighted-average pressure ratio across the combustor in Figure 7 is 15.78, significantly higher than the sharp-wedge counterpart.

However, there are some benefits of the blunted wedge in the combustor. The induction region is an inconsequential concept for the blunted case, which provides an opportunity to utilize a very short wedge in the combustor. This contrasts with a sharp wedge counterpart, where the wedge length must be greater than the ODW induction region length (around 30 mm for the case
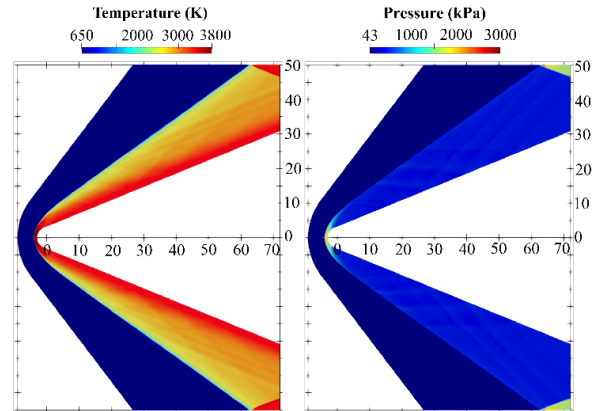
in Figure 6). The instantaneous ignition with a blunt wedge also ensures that the combustor is relatively less susceptible to the inflow mixture inhomogeneity and fluctuations of flow parameters the mixture will consistently ignite at the stagnation region due to its high temperature. Moreover, as discussed previously, a practical wedge will have a finite bluntness, hence, the sharp-wedge result is an idealized scenario. Therefore, the blunt wedge result in Figure 7 provides a better picture of the phenomena that can exist in a real ODWE combustor.

The applications above demonstrate the utility of the current flow solver in a fundamental study as well as in the design of a hypersonic propulsion system. The reliability of the solver in the prediction of the high temperature and low Mach number stagnation region shows that the solver is reliable as an analysis tool of the practical ODWE combustors.

5. Conclusion

An OpenFOAM solver, hRSF, was developed by incorporating new reconstruction methods previously used in *rhoCentralFoam* [3]. This method was adopted for all primitive variables in the generic Riemann flux class. This reconstruction technique ensures the successful implementation of TVD property in the numerical simulation. Similarly, to increase the spatial accuracy order of species density flux to second order, species fluxes were computed using the Riemann scheme in the generic Riemann class code, which mitigates the issues present in the previous version of the current solver. The validation cases presented in this study clearly showed that the solver can fully resolve both overdriven and underdriven detonation cases in blunt bodies. The solver precisely captures the bow shock and the reaction front. Comparative plots between two computational results show the capability of the current solver to compute shock

stand-off distance precisely. Similarly, experimental and numerical results for hypersonic blunt body projectile compare closely, which builds high confidence in the further usage of the current solver for computation of supersonic/hypersonic reacting flows. It was observed that despite the current solver's capability, there is still room for further development regarding the accuracy of time integration. The addition of time integration methods will potentially resolve the formation of small kink structures in underdriven, highly transient cases. However, the issues present do not limit the usage of the solver for the computation of detonation cases for sharp as well as blunted wedges. The combustors with sharp wedges provide better total pressure recovery in comparison to the blunted wedge cases. However, blunted wedge depicts the actual detonation phenomenon that forms in practical ODWE as every physically manufactured sharp wedge has a finite bluntness during manufacturing and materials limitations. It can be concluded that for research and development of practical ODWEs, future studies should consider finite bluntness in combustor wedges to demonstrate the actual detonation phenomenon.

Acknowledgemant

Conflict of interest

No conflict of interest

References

[1] Bhattrai S, Tang H. Formation of near-chapman– jouguet oblique detonation wave over a dual-angle ramp[J/OL]. Aerospace Science and Technology, 2017, 63: 1-8. DOI: https://doi.org/10.1016/j.ast.2016.12.010.

[2] Bomjan B, Bhattrai S, Tang H. Characterization of induction and transition methods of oblique detonation waves over dual-angle wedge[J/OL]. Aerospace Science and Technology, 2018, 82: 394-401. DOI: https://doi.org/10.1016/j.ast.2018.07.038.

[3] Greenshields C J, Weller H G, Gasparini L, et al. Implementation of semi-discrete, non-staggered central schemes in a colocated, polyhedral, finite volume framework, for high-speed viscous flows[J/OL]. International journal for numerical methods in fluids, 2010, 63(1): 1-21. DOI: https://doi.org/10.1002/fld.2069.

[4] Ettner F, Vollmer K G, Sattelmayer T. Numerical simulation of the deflagration-to-detonation transition in inhomogeneous mixtures[J/OL]. Journal of Combustion, 2014, 2014. DOI: https://doi.org/10.1155/2014/686347.

[5] Borm O, Jemcov A, Kau H P. Density based navier stokes solver for transonic flows[M/OL]. In Proceedings of 6th OpenFOAM workshop, penn state university, USA, 2011. http://www.appliedccm.com/wp-content/uploads/2015/07/oliver_borm_slides.pdf.

[6] Rosato D A, Thornton M, Sosa J, et al. Stabilized detonation for hypersonic propulsion[J/OL]. Proceedings of the National Academy of Sciences, 2021, 118(20). DOI: https://doi.org/10.1073/pnas.2102244118.

[7] Dabora. E K, Desbordes D, Guerraud C, et al. Oblique detonation at hypersonic velocities[J]. Progress in Astronautics and Aeronautics, 1991, 133: 187-201.

[8] Viguier C, Gourara A, Desbordes D. Three- dimensional structure of stabilization of oblique detonation wave in hypersonic flow[J/OL]. In Symposium (International) on Combustion, 1998, 27(2): 2207-2214. DOI: https://doi.org/10.1016/S0082-0784(98/80069-6).

[9] Li C, Kailasanath K, Oran E S. Detonation structures behind oblique shocks[J/OL]. Physics of Fluids, 1994, 6(4): 1600-1611. DOI: https://doi.org/10.1063/1.868273.

[10] Silva D, Figueria L F, Deshaies B. Stabilization of an oblique detonation wave by a wedge: a parametric numerical study[J/OL]. Combustion and Flame, 2000, 121(1-2): 152-166. DOI: https://doi.org/10.1016/S0010-2180(99/00141-8).

[11] Papalexandris M V. A numerical study of wedge-induced detonations[J/OL]. Combustion and flame, 2000, 120(4): 526-538. DOI: https://doi.org/10.1016/S0010-2180(99/00113-3).

[12] Pimentel C A R, Azevedo J L F, Figueira L F, et al. Numerical study of wedge supported oblique shock wave-oblique detonation wave transitions[J/OL]. Journal of the Brazilian Society of Mechanical Sciences, 2002, 24: 149-157. DOI: https://doi.org/10.1590/S0100-73862002000300002.

[13] Xiang G, Li X, Sun X, et al. Investigations on oblique detonations induced by a finite wedge in high altitude[J/OL]. Aerospace Science and Technology, 2019, 95: 105451. DOI: https://doi.org/10.1016/j.ast.2019.105451.

[14] Brackett D C, Bogdanoff D W. Computational investigation of oblique detonation ramjet-in-tube concepts[J/OL]. Journal of Propulsion and Power, 1989, 5(3): 276-281. DOI: https://doi.org/10.2514/3.23149.

[15] Hertzberg A, Bruckner A P, Knowlen C. Experimental investigation of ram accelerator propulsion modes[J/OL]. Shock Waves, 1991, 1(1): 17-25. DOI: https://doi.org/10.1007/BF01414864.

[16] Li C, Kailasanath K, Oran E S. Detonation structures generated by multiple shocks on ram- accelerator projectiles[J/OL]. Combustion and Flame, 1997, 108(1-2): 173-186. DOI: https://doi.org/10.1016/S0010-2180(96/00102-2).

[17] Sislian J P, Dudebout R, Schumacher J, et al. Incomplete mixing and off-design effects on shock-induced combustion ramjet performance[J/OL]. Journal of Propulsion and Power, 2000, 16(1): 41-48. DOI: https://doi.org/10.2514/2.5529.

[18] Hong-Hui T, Wei Z, Zong-Lin J. A novel oblique detonation structure and its stability[J/OL]. Chinese Physics Letters, 2007, 24(7): 1985. DOI: https://doi.org/10.1088/0256-307x/24/7/055.

[19] Miao S, Zhou J, Liu S, et al. Formation mechanisms and characterisics of transition patterns in oblique detonations[J/OL]. Acta Astronautica, 2018, 142: 121-129. DOI: https://doi.org/10.1016/j.actaastro.2017.10.035.

[20] Teng H, Zhang Y, Jiang Z. Numerical investigation on the induction zone structure of the oblique detonation waves[J/OL]. Computers Fluids, 2014, 95: 127-131. DOI: https://doi.org/10.1016/j.compfluid.2014.03.001.

[21] Verreault J, Higgins A J. Initiation of detonation by conical projectiles[C/OL]// Proceedings of the Combustion Institute: volume 33. 2011: 2311-2318. DOI: https://doi.org/10.1016/j.proci.2010.07.086.

[22] Fujiwara T, Matsuo A, Nomoto H. A two- dimensional detonation supported by a blunt body or a wedge[J/OL]. In 26th Aerospace Sciences Meeting, 1988: 98. DOI: https://doi.org/10.2514/6.1988-98.

[23] Fang Y, Zhang Z, Hu Z, et al. Initiation of oblique detonation waves induced by a blunt wedge in stoichiometric hydrogen-air mixtures[J/OL]. Aerospace Science and Technology, 2019, 92: 676-684. DOI: https://doi.org/10.1016/j.ast.2019.06.031.

[24] Lehr H F. Experiments on shock-induced combustion[J/OL]. Astronautica Acta, 1972, 17: 589-597. https://ci.nii.ac.jp/naid/10003489385/.

[25] McVey J B, Toong T Y. Mechanism of instabilities of exothermic hypersonic blunt-body flows[J/OL]. Combustion Science and Technology, 1971, 3(2): 63-76. DOI: https://doi.org/10.1080/00102207108952273.

[26] Matsuo A, Fujiwara T. Numerical investigation of oscillatory instability in shock-induced combustion around a blunt body[J/OL]. AIAA journal, 1993, 31(10): 1835-1841. DOI: https://doi.org/10.2514/3.11856.

[27] Ahuja J, Tiwari S, Kumar A. Numerical investigation of shock-induced combustion past blunt projectiles in regular and large-disturbance regimes[J/OL]. In 33rd Aerospace Sciences Meeting and Exhibit, 1995: 153. DOI: https://doi.org/10.2514/6.1995-153.

[28] Wilson G J, MacCormack R W. Modeling supersonic combustion using a fully implicit numerical method[J/OL]. AIAA journal, 1992, 30(4): 1008-1015. DOI: https://doi.org/10.2514/3.11021.

[29] Yungster S, Eberhardt S, Bruckner A. Numerical simulation of shock-induced combustion generated by high-speed projectiles in detonable gas mixtures[J/OL]. In 27th Aerospace Sciences Meeting, 1989: 673. DOI: https://doi.org/10.2514/6.1989-673.

[30] Choi J Y, Jeung I S, Yoon Y. Computational fluid dynamics algorithms for unsteady shock-induced combustion, part 1: validation[J/OL]. AIAA journal, 2000, 38(7): 1179-1187. DOI: https://doi.org/10.2514/2.1112.

[31] Jachimowski C J. An analytical study of the hydrogen-air reaction mechanism with application to scramjet combustion[EB/OL]. 1988. https://ntrs.nasa.gov/citations/19880006464.

[32] Liou M S. A sequel to ausm, part ii: Ausm+-up for all speeds[J/OL]. Journal of computational physics, 2006, 214(1): 137-170. DOI: https://doi.org/10.1016/j.jcp.2005.09.020.

[33] Kee R J, Rupley F M, Miller J A. Chemkin-ii: A fortran chemical kinetics package for the 260 analysis of gas-phase chemical kinetics[EB/OL]. 1989. DOI: https://doi.org/10.2172/5681118.

[34] Roe P L. Characteristic-based schemes for the euler equations[J]. Annual review of fluid mechanics, 1986, 18(1): 337-365.